Title

Microdosimetric Analysis for Boron Neutron Capture Therapy via Monte Carlo Track Structure Simulation with Modified Lithium Cross-sections.

Permalink

https://escholarship.org/uc/item/8ng6d8nj

Authors

Han, Yang

Geng, Changran

D-Kondo, J

et al.

Peer reviewed

Microdosimetric Analysis for Boron Neutron Capture Therapy via Monte Carlo Track Structure Simulation with Modified Lithium Cross-sections

Yang Han[1,2,3], **Changran Geng**[1,2,*], **J. Naoki D-Kondo**[4], **Mingzhu Li**[1,2], **José Ramos-Méndez**[4], **Saverio Altieri**[3,5], **Yuanhao Liu**[1,2], **Xiaobin Tang**[1,2,*]

[1]Nanjing University of Aeronautics and Astronautics, Department of Nuclear Science and Technology, Nanjing, 210016, China

[2]Joint International Research Laboratory on Advanced Particle Therapy, Nanjing 211100, China

[3]University of Pavia, Department of Physics, Pavia, 27100, Italy

[4]University of California San Francisco, Department of Radiation Oncology, San Francisco, CA 94115, USA

[5]Istituto Nazionale di Fisica Nucleare (INFN), the section of Pavia, Pavia, 27100, Italy

Abstract

Boron neutron capture therapy (BNCT) is a cellular-level hadron therapy achieving therapeutic effects via the synergistic action of multiple particles, including Lithium, alpha, proton, and photon. However, evaluating the relative biological effectiveness (RBE) in BNCT remains challenging. In this research, we performed a microdosimetric calculation for BNCT using the Monte Carlo track structure (MCTS) simulation toolkit, TOPAS-nBio. This paper reports the first attempt to derive the ionization cross-sections of low-energy (>0.025 MeV/u) Lithium for MCTS simulation based on the effective charge cross-section scalation method and phenomenological double-parameter modification. The fitting parameters ($\lambda_1 = 1.101$, $\lambda_2 = 3.486$) were determined to reproduce the range and stopping power data from the ICRU report 73. Besides, the lineal energy spectra of charged particles in BNCT were calculated, and the influence of sensitive volume (SV) size was discussed. Condensed history simulation obtained similar results with MCTS when

using Micron-SV while overestimating the lineal energy when using Nano-SV. Furthermore, we found that the microscopic boron distribution can significantly affect the lineal energy for Lithium, while the effect for alpha is minimal. Similar results to the published data by PHITS simulation were observed for the compound particles and monoenergetic protons when using micron-SV. Spectra with nano-SV reflected that the different track densities and absorbed doses in the nucleus together result in the dramatic difference in the macroscopic biological response of BPA and BSH. This work and the developed methodology could impact the research fields in BNCT where understanding radiation effects is crucial, such as the treatment planning system, source evaluation, and new boron drug development.

Keywords

Boron neutron capture therapy; Microdosimetry; Lineal energy; Monte Carlo track structure simulation

1   Introduction

Boron neutron capture therapy (BNCT) is a binary targeted cancer treatment that takes advantage of the large neutron capture cross-sections of ^{10}B and the short range of secondary particles, enabling it to be one of the most effective therapeutic modalities for the locally invasive malignancies (Matsumoto et al., 2021; Moss, 2014; Suzuki, 2020). In the boron neutron capture reactions, 1.47 MeV alpha, 0.84 MeV Lithium (^{7}Li), and 0.478 MeV photon are produced with 93.7% probability, whereas the remaining 6.3% probability of emitting 1.77 MeV alpha and 1.02 MeV Lithium. In addition, 0.58 MeV monoenergetic protons from the ^{14}N(n,p)^{14}C reaction, recoil protons from the ^{1}H(n,n)p reaction, photons from the ^{1}H(n,γ)^{2}H reaction, and contaminating photons also delivered considerable additional dose to tumor and tissue during the treatment (Hopewell et al., 2011). In the treatment planning system for BNCT, different relative biological effectiveness (RBE) or compound biological effectiveness (CBE) are used to evaluate the dose contribution of different particle components (Wu et al., 2020). However, these RBEs or CBEs are mostly empirical conclusions derived from animal or cell experiments (Fukuda, 2021). Few microdosimetric studies have attempted to describe the mechanism of biological effects produced by different particles in BNCT, thereby limiting the accuracy of effectiveness projection.

Most microdosimetric experiments in BNCT have been performed by adding boron in the cathode plastic of the tissue equivalent proportional counters (TEPCs) (Burmeister et al., 2001; Colautti et al., 2014; Hu et al., 2020a; Hu et al., 2020b; Selva et al., 2022) or on the surfaces of the silicon microdosimeters (Hu et al., 2018). However, this approach differs from the actual situation in terms of microscopic boron distribution and its scale (Mukawa et al., 2011). Therefore, Monte Carlo simulation which can support the low-energy particle transport is an effective method for analyzing the specific microdosimetric characteristics. Researchers from Japan Atomic Energy Agency have performed many related studies using PHITS software (Furuta and Sato, 2021; Horiguchi et al., 2015; Sato et al., 2018). These studies used Monte Carlo condensed history (MCCH) algorithm rather than Monte

Carlo track structure (MCTS) simulation (Lazarakis et al., 2018). MCCH "groups" many interactions of charged particles along artificial steps and is valid (or recommended) above 250 eV of incoming kinetic energy. Although some results obtained by MCCH are similar to MCTS by setting a small step size and production cut, its validity still needs further verification when reaching DNA level (Kyriakou et al., 2017; Kyriakou et al., 2019; Kyriakou et al., 2021a). In the latest study, PHITS-KURBUC has also started to support the MCTS simulation for electron, proton, and carbon ion in liquid water, but it has not included the main charged particles in BNCT (Matsuya et al., 2022). Geant4-DNA is an open-source software which supports MCTS simulation for electrons, photons and ions (Bernal et al., 2015; Incerti et al., 2010a; Incerti et al., 2010b; Incerti et al., 2018). However, limited by the lack of experimental data and theoretical models, Geant4-DNA performs a rough handling of the ionization cross-sections of ions with energy lower than 0.5 MeV/u in "G4EmDNAphysics", introducing the challenge of the track structure simulation for Lithium in BNCT (Qi et al., 2021).

In this study, we conducted a microsimetric simulation including all of the essential particles in BNCT. The software used in this work was TOPAS 3.7 and TOPAS-nBio 1.0 (Schuemann et al., 2019), built on the framework of Geant4-DNA. Given the limitations of the current "G4EmDNAphysics" on ionization transport of ions, we performed the first attempt to derive the ionization cross-sections of low-energy Lithium for MCTS simulation in BNCT based on the effective charge cross-section scalation method and phenomenological double-parameter modification. Then, we verified the range and stopping power of Lithium, alpha, and proton with a similar energy scope in BNCT to ensure the applicability of the physics models and cross-sections in this work. Finally, we performed the calculation for the lineal energy spectra and analysis for the influence of sensitive volume (SV) size with two types of boron heterogeneity distributions, ^{10}B-boronphenylalanine (BPA, $C_9H_{12}BNO_4$) and ^{10}B-sodium (BSH, $Na_2[B_{12}H_{11}SH]$).

2 Materials and methods

2.1 Physics models and cross-sections

The physics list applied to this research is named "TsEmDNAphysics" in TOPAS-nBio which allows to customize physics models per process. The details of the physics models and energy cut-off are listed in Table 1.

The cross-section modification for Lithium is the key to performing MCTS simulations in BNCT. In Geant4-DNA, ionization cross-sections for ions heavier than alphas are calculated using a scaling method described by Francis et al. (Francis et al., 2011) that relies on the proton cross-sections. However, this scaling procedure is only recommended for ions with energies above 0.5 MeV/u, because the predominance of charge-exchange and excitation processes are not considered in this scaling. As a result, the stopping power and range mismatch from the published data (Islam et al., 2017). In this work, we followed the procedure published by Schmitt et al. (Schmitt et al., 2015) in which the ionization cross-sections for heavier ions than alphas were calculated from a weighted linear combination of the ionization cross-sections for proton and hydrogen according to the Barkas scaling (Barkas, 1963). However, the Barkas scaling of the Geant4-DNA cross-sections still did

not recreate the data from International Commission on Radiation Units & Measurements report 73 (ICRU_73) (Sigmund et al., 2005) for Lithium. Hence, accompanying Eq. (1), two additional empirical parameters λ_1 and λ_2 were introduced and adjusted to fit the data from ICRU_73. To choose the best λ_1 and λ_2 in an unbiased manner, we relied on a Nelder-Mead algorithm described elsewhere (D-Kondo et al., 2021; Nelder, 1965).

The effective charge cross-section scalation method and phenomenological double-parameter modification can be described by Eq. (1):

$$\sigma_Z(v) = \frac{\left(\lambda_1 \sigma_p(v) \gamma_1(v) \ + \ \lambda_2 \sigma_H(v)(1 - \gamma_1(v))\right) Z^2 \gamma_Z(v)^2}{\gamma_1(v)^2},\tag{1}$$

where $\sigma_Z(v)$ is the ionization cross-sections of ion with atomic number Z and speed v, λ_1 and λ_2 are two phenomenological adjustment parameters, $\sigma_p(v)$ and $\sigma_H(v)$ are the ionization cross-sections for proton and hydrogen, $\gamma_z(v)$ is the Barkas effective charge factor expressed in Eq. (2):

$$\gamma_Z(v) = 1 - \exp\left(-125\left(\frac{v}{c}\right) Z^{-\frac{2}{3}}\right),\tag{2}$$

$\gamma_1(v)$ is the effective charge factor for hydrogen whose atomic number is 1, expressed in Eq. (3):

$$\gamma_1(v) = 1 - \exp\left(-125\left(\frac{v}{c}\right)\right).\tag{3}$$

The values of λ_1 and λ_2 used for Lithium in this work were determined to be 1.101 and 3.486, respectively, to recreate the range and stopping power data from ICRU 73. The modified cross-sections can be used by Topas-nBio through the physics model called "TsDNARuddIonisationExtendedModel" as shown in Table 1, thus allowing for the transport of Lithium with energy higher than 0.025 MeV/u. For the other particles, "TsEmDNAphysics" executes the same physics models as "G4EmDNAphysics_option2".

2.2 Cross-section verification

During the verification process for the cross-sections used in this work, we constructed a sufficiently large water sphere in which particles were emitted homogeneously from the center. The initial particles selected for verification were [7]Li (0.21–1.75 MeV), alpha (0.001–2 MeV), and proton (0.03–10 MeV). The energy scopes of particles comprehensively considered the BNCT environment.

Range and stopping power were adopted as the main indicators for evaluating the accuracy of the cross-sections in this study. Here, range is defined as the line segment distance of the charged particles with the kinetic energy reduced to 0.025 MeV/u. For stopping power, we used the "stationary" physical processes to ensure that the particle energy of each step is guaranteed to remain at the initial energy under the condition of killing the

secondary electrons and photons, which refers to the Geant4-DNA example "spower". The main reference data for Lithium comes from ICRU_73, while the reference data for alpha and proton were obtained from ICRU_90 (Seltzer et al., 2016).

2.3   Lineal energy calculation

2.3.1   Geometry—Although the particles acting mainly in BNCT have a short range (μm), the influence from neighboring cells and intercellular medium still need to be considered. Here, we designed a water phantom containing 3*3*3 cells, as shown in Figure 1. Each cell included a membrane, cytoplasm, and nucleus. The cell and nucleus radii were set to 5 and 2.5 μm, respectively (Sato et al., 2018). The thickness of the cell membrane was set to 8 nm. To ensure that the effects of neighboring cells have been taken into account, we performed the lineal energy counts only in the central cell nucleus, marked by orange in Figure 1.

2.3.2   Particle source—On the basis of the various original processes and ranges of the particles in BNCT, we designed the particle sources with different spatial distributions to match the actual situation. For the monoenergetic proton, which originates from the nitrogen neutron capture reaction, the energy is kept at 0.58 MeV with the corresponding range of less than 10 μm. Therefore, the isotropic monoenergetic proton source was set uniformly in a cube with 30 μm side length. Since the counting area is in the center nucleus (2.5 μm radius sphere), which is much smaller than the proton source volume, the effect of the shape of isotropic source is minimal. For the recoil proton, which originates from the hydrogen nucleus elastic scattering, the energy scope is mainly from 10^{-3} to 1 MeV. Therefore, the isotropic recoil proton source was set uniformly in a cube with 100 μm side length. The energy spectrum of the recoil proton can be derived from our previous work (i.e., MIT recoil proton spectrum) (Qi et al., 2021). For the alpha particle, which originates from the boron neutron capture reaction, the energy is 1.77 MeV (6.3%) and 1.47 MeV (93.7%). Its spatial distribution is related to the microscopic distribution of boron drugs and neutron flux, but the latter has little effect because the neutron flux almost has no change at the (sub) cellular scale. Therefore, we set three isotropic particle source patterns in this research: uniformly enriched in the intercellular (*Ic*), cytoplasm (*Cy*), and cell membrane (*Cm*). For Lithium, the spatial distribution is the same as alpha, but the energy was set to 1.02 MeV (6.3%) and 0.84 MeV (93.7%) in accordance with the probability of the BNCT reaction channel.

2.3.3   Lineal energy analysis—Lineal energy (y) is defined as the ratio of energy imparted (ε_s) (i.e., energy deposition in SV for each event s) and the mean chord length ($\overline{l}$) (i.e., 2/3 of the SV diameter) in SV. The lower and upper limits of lineal energy were set to 0.1 and 10000 keV/μm, respectively. Two types of SV were used in this work, i.e., nano-SV with radius equal to 1 nm and micron-SV with radius equal to 2.5 μm. Figure 2 shows the schematic of lineal energy calculation.

For nano-SV, the counting area is in the central nucleus. The lineal energy spectrum was determined by the following processes (Kyriakou et al., 2017):

1.   Let an event s be defined as a primary particle and all its secondary particles;

2. Follow the event and record the information of each step in the counting area;

3. Select one step randomly;

4. Find one SV center whose distance to the selected step is less than 1 nm;

5. Specify a sphere (i.e., SV) of 1 nm radius with the SV center;

6. Calculate the energy deposition in the SV and determine the lineal energy with the associated statistical weight;

7. Repeat (3)~(6) and the number of repetitions (i.e., the number of SVs) is proportional to the number of steps in the counting area;

8. Repeat (1)~(7) for the next event.

For micron-SV, the counting area is in the central nucleus and the SV is the same as the counting area.

We used $yf(y)$ and $yd(y)$ to describe the lineal energy's frequency and dose contribution spectrum. The relationship between $f(y)$ and $d(y)$ is shown in Eq. (4):

$$d(y) = \frac{yf(y)}{\int_0^\infty yf(y)dy}.$$

(4)

The frequency-mean lineal energy ($\bar{y}_F$) and dose-mean lineal energy ($\bar{y}_D$) were calculated according to Eqs. (5) and (6):

$$\bar{y}_F = \int_0^\infty yf(y)dy,$$

(5)

$$\bar{y}_D = \int_0^\infty yd(y)dy = \frac{\int_0^\infty y^2 f(y)dy}{\int_0^\infty yf(y)dy}.$$

(6)

Clinically, the absorbed dose of boron neutron capture (BNC) reaction (i.e., boron dose) needs to be calculated, and CBE is used to describe the biological response to the boron dose (including Lithium and alpha). Therefore, the lineal energy results of the compound particles were determined by the weighting process described in this section. Under the assumption that the boron drug cannot enter the nucleus (Sato et al., 2018), ions that shoot into the nucleus can be considered mutually independent events since the BNCT reaction produces alpha and Lithium with opposite momentum. In addition, we need to weight the microscopic boron distribution to match the actual inhomogeneous microscopic boron distribution. The lineal energy frequency of the compound particles ($f(y)_{BNC}^j$) was thus determined by Eq. (7):

$$f(y)_{BNC}^j = \frac{\sum_{i,k} M_k^i Q^{i,j} f(y)_k^i}{\sum_{i,k} M_k^i Q^{i,j}},$$

(7)

where *M* is the fraction of initial primary ions which reach the counting area and deposit energy within SV, *Q* is the boron distribution factor, *i* represents the source condition (i.e., *Ic*, *Cy*, and *Cm*), j represents the boron carrier (i.e., BPA and BSH), k represents the particle type (i.e., alpha and Lithium). The weighting factors are listed in Table 2. The boron weighting factors were determined based on the boron concentration data of malignant cells (Capala et al., 1996) and the cell size (Sato et al., 2018).

3 Results

3.1 Range and stopping power verification

To ensure the accuracy of the track structure simulation in the BNCT environment, we first verified that the particle range and the stopping power using the specific physics models and cross-sections are consistent with the ICRU reports, as described in Section 2.2.

For Lithium, we adopted the physics list named "TsEmDNAphysics" including the specific model for ions "TsRuddIonisationExtendedModel" which invokes the new Lithium cross-sections, hereafter named "Rudd_new". We compared the results of ICRU_73, "Rudd_new", "Rudd_original" (the original Rudd cross-sections of Lithium from Geant4-DNA), "Penelope/Livermore" (MCCH, step size = 1 nm, production cut = 0.0001 eV). As shown in Figure 3, the best match is found between "Rudd_new" and ICRU_73 in terms of range and stopping power. The results given by "Rudd_original" show the worst consistency, especially when the particles have lower energies. The main reason for this phenomenon is the higher probability of charge exchange in the low-energy region and the fact that excitation is not considered in "Rudd_original". "Penelope/Livermore" gives a similar tendency to the data from ICRU_73, but with lower stopping power and longer range.

For alpha and proton, we compared the range and stopping power obtained with our physics module, "TsEmDNAphysics" or "TsEmDNAphysics_stationary", with data from ICRU_90. For computing stopping power, the "TsEmDNAphysics_stationary" module uses a frozen-velocity approximation which keeps artificially constant the incident particle kinetic energy at each step. In this way, the stopping power is correctly calculated according to its definition (Incerti et al., 2018). The results are shown in Figure 4. The close agreement demonstrates the ability of our MCTS code to sufficiently accomplish the track structure simulation for low-energy charged particles in BNCT.

3.2 Lineal energy spectra

3.2.1 Lineal energy spectra of proton in BNCT—The lineal energy spectra of protons are presented in Figure 5. Figures 5(a) and (b) show the results when SV radius is equal to 1 nm (i.e., nano-SV), while Figures 5(c) and (d) show the results when SV radius is equal to 2.5 μm (i.e., micron-SV). The left plots give the frequency spectra (i.e., $yf(y)$), while the right plots give the dose contribution spectra (i.e., $yd(y)$). The solid line represents the results of MCTS, and the color block represents the result of MCCH (G4-Livermore). Red represents the results of monoenergetic protons (from $^{14}N(n,p)^{14}C$ reaction), and blue represents the results of recoil protons (from $^{1}H(n,n)p$ reaction). Green points are data from

the published work by T. Sato et al. (Sato et al., 2018) through PHITS simulation. The corresponding frequency-mean lineal energy ($\bar{y}_F$) and dose-mean lineal energy ($\bar{y}_D$) are listed in Table 3.

Comparing the results of MCTS and MCCH, we find that with nano-SV, the MCCH results have a higher probability at high lineal energy region, both in the $yf(y)$ and $yd(y)$ plots. The different mean values shown in Table 3 suggest that MCCH may introduce a considerable overestimation of $\bar{y}_F$ and $\bar{y}_D$ when using nano-SV, even though we have set fairly conservative parameters for MCCH simulation (i.e., step size =0.1 nm, tracking and production cut = 0.0001 eV). However, in the low lineal energy region of the $yf(y)$ diagram, MCTS gives much higher probabilities than MCCH. These counts come from the excitation of secondary electrons (Thompson et al., 2022), which indirectly illustrates the advantage of MCTS simulation for accurate low-energy particle transport at the nanoscale. Of course, these counts have little effect on the dose contribution spectrum, which is frequently used to establish a relationship to biological response. When using micron-SV, our calculated MCCH (G4-Livermore) results and those calculated by PHITS (MCCH) are very similar to the MCTS results. The laws are analogous to the conclusion on electrons declared by I. Kyriakou et al. (Kyriakou et al., 2019). Considering that MCTS is more refined for nanoscale simulations, we will focus on MCTS-based microdosimetric analysis of BNCT-related particles in the subsequent sections, and the results obtained by G4-Livermore (MCCH) will not be presented and discussed.

When the SV radius is 1 nm, the dose-mean lineal energy of the monoenergetic proton and recoil proton is 52.40 and 41.35 keV/μm, respectively. The lower $\bar{y}_D$ value of recoil proton is due to the recoil proton spectrum containing a large number of protons with lower ionization capacity. When the SV radius is 2.5 μm, the recoil proton makes a lower $\bar{y}_D$ value than the monoenergetic proton, which is the same as the nano-SV cases.

In addition, comparing the lineal energy distribution with micron-SV and nano-SV, we find that the dose contribution spectrum obtained with nano-SV has a broader scope of the peak than the micron-SV case, but they get a similar $\bar{y}_D$, reflecting the statistical rise and fall of the lineal energy at the nanometer scale. D. Mazzucconi et al. also found an analogous lineal energy distribution with different SV sizes in external proton irradiation (Mazzucconi et al., 2019a).

3.2.2 Lineal energy spectra of particles related to the BNC reaction

(1)   Lithium: The emission distribution of Lithium in BNCT is related to the microscopic boron accumulation. In this study, we set three ideal spatial distribution source patterns to calculate the lineal energy spectra in the cell nucleus, marked by , Cy, and Cm. The lineal energy spectra of Lithium are presented in Figure 6. Figure 6(a) and (b) show the results when SV radius is equal to 1 nm (i.e., nano-SV), while Figure 6(c) and (d) show the results when SV radius is equal to 2.5 μm (i.e., micron-SV). The left plots give the frequency spectra (i.e., $yf(y)$), and the right plots give the dose contribution spectra (i.e., $yd(y)$). Solid lines with different colors represent the spectra under different source conditions (i.e.,

red: Cy, blue: Cm, purple: Ic). The corresponding frequency-mean lineal energy ($\bar{y}_F$) and dose-mean lineal energy ($\bar{y}_D$) are presented in Table 4.

When the SV radius is 1 nm, Figure 6(a) shows a relatively high frequency on the low lineal energy part. These counts come from sparse electron steps away from the primary ion track, with minimal steps and energy deposition in the SV. Peaks at several keV/μm could be attributed to the transition energies of the excitation levels and the binding energies of the ionization shells, occurring when the incident and secondary electrons excite or ionize liquid water molecules. Nevertheless, these counts have little effect on the dose contribution spectrum because their dose percentage is tiny. Besides, the dose contribution spectra of lineal energy (Figure 6(b)) illustrates that the lineal energy is more concentrated at the high-value region under the Cy condition, causing a higher $\bar{y}_D$ than the Cm and Ic condition. This difference is because the Lithium emitted in BNCT is 0.84 MeV (93.7%), which has the almost highest ionization ability for Lithium, reflected by the stopping power curve shown in Figure 3(b). Lithium particles emitted under the Cy condition are closer to the nucleus, so reach the nucleus with higher residual energy and ionization capacity.

When the SV radius is 2.5 μm, more significant differences are observed under different source conditions. This is because the range of Lithium is about 3 μm, which make it difficult to penetrate the cytoplasm and nucleus, inducing the lower energy deposition in the nucleus under the Ic and Cm conditions. This difference is minor in the case of nano-SV because nano-SV is much easier to penetrate and its position is adjusted by step rather than fixed in the nucleus, as shown in Figure 2.

__(2)   Alpha:__ The lineal energy spectra of alpha are presented in Figure 7. Figures 7(a) and (b) show the results when SV radius is equal to 1 nm (i.e., nano-SV), while Figures 7(c) and (d) show the results when SV radius is equal to 2.5 μm (i.e., micron-SV). The left plots give the frequency spectra (i.e., $yf(y)$), and the right plots give the dose contribution spectra (i.e., $yd(y)$). Solid lines with different colors represent the spectra under different source conditions (i.e., red: Cy, blue: Cm, purple: Ic). The corresponding frequency-mean lineal energy ($\bar{y}_F$) and dose-mean lineal energy ($\bar{y}_D$) are listed in Table 4.

When the SV radius is 1 nm, the lineal energy distributions under different source conditions are more similar for alpha, compared to the Lithium case. This phenomenon is because the emission energy of alpha in BNCT is 1.47 MeV (93.7%). The stopping power of alpha increases (>0.7 MeV) and then decreases (0~0.7 MeV) with decreasing energy, as shown in Figure 4(b), rather than the monotonic pattern for Lithium (<0.84 MeV). Overall similar ionization abilities and lineal energy distributions are constructed because charged particles have a broad energy scope when they reach the cell nucleus. Nevertheless, the value of $\bar{y}_D$ under the Cy condition of alpha is the smallest, compared to the Cm and Ic conditions, which is opposite to the pattern of Lithium with nano-SV.

However, when the SV radius is 2.5 μm, we find that the law of $\bar{y}_D$ for alpha particles still obeys $Cy > Cm > Ic$, the same as Lithium. This phenomenon indicates that although the track density of each event in the nucleus is similar under different source conditions for

alpha, the energy depositions of each event in the nucleus are different and show a similar pattern to Lithium. Moreover, compared to the vastly different lineal energy distribution exhibited by Lithium with micron-SV under different source conditions, the difference is smaller for alpha. This is because the range of alpha produced in BNCT is about 7 μm, which means alpha can penetrate the cytoplasm and nucleus more easily.

Furthermore, comparing the $yd(y)$ plots with nano-SV and micron-SV, the peak with nano-SV is broader because of the more significant stochasticity in the track density at the nanoscale. In our work, the dose-mean lineal energy is larger when using micron-SV than nano-SV for alpha, which is also consistent with the published research by external helium irradiation (Mazzucconi et al., 2019b).

(3) Compound particles: The lineal energy spectra for the compound particles are presented in Figure 8. Figures 8 (a) and (b) show the results when SV radius is equal to 1 nm (i.e., nano-SV), while Figures 8(c) and (d) show the results when SV radius is equal to 2.5 μm (i.e., micron-SV). The left plots give the frequency spectra (i.e., $yf(y)$), and the right plots give the dose contribution spectra (i.e., $yd(y)$). Different colors represent the results under different microscopic boron distributions and data by PHITS simulation (Sato et al., 2018) (i.e., red line: BPA this work, blue line: BSH this work, green point: BPA PHITS, purple point: BSH PHITS). The corresponding frequency-mean lineal energy ($\bar{y}_F$) and dose-mean lineal energy ($\bar{y}_D$) are presented in Table 5.

When the SV radius is 1 nm, the dose-mean lineal energy of the compound particles is 158.35 and 132.47 keV/μm for BPA and BSH, respectively. The shape of the lineal energy distribution of the compound particles is similar to that of the "pure alpha", as shown in Figure 7. This is because alpha particles have a long range and can penetrate the cytoplasm more easily, so they make up the main part of the compound particles in the nucleus. The difference between BPA and BSH shown on the $yd(y)$ diagram mainly comes from the influence of Lithium. Since the emission site of Lithium is closer to the nucleus under the BPA condition, the influence of its short range is alleviated, and thus Lithium exerts a more significant effect. As a result, a concentration of counts at a higher lineal energy region for BPA is found in Figure 7(b). Some researchers stated that the higher the dose-mean lineal energy, the higher the RBE, when $\bar{y}_D$ is less than 200 keV/μm (Parisi et al., 2022). However, considering the overkill effect, there is no consensus on this extreme point of the RBE-LET/$\bar{y}_D$ curve, which also seems to be different for different charged particles. Therefore, in this work, we can only speculate that the RBE of BPA might be higher than that of BSH. The biological response requires the RBE multiplied by the absorbed dose. For BNCT, the intranuclear absorbed dose varies considerably due to the inhomogeneity of the microscopic boron distribution and the short ion range. Further studies are needed to quantify the biological response.

When the SV radius is 2.5 μm, the results generally agree with those obtained by PHITS, indicating that the difference between the MCCH and MCTS methods is slight for the microdosimetric analysis with micron-SV, which has been explained in Section 3.1.1. Besides, the difference between lineal energy distributions for BPA and BSH is tiny. The

conclusions obtained from the micron-SV study are more inclined to suggest that the RBE of BPA and BSH are identical at the micron scale, and only the difference in the intranuclear absorbed dose leads to the different macroscopic biological response of these two drugs.

Comparing the results of the nano-SV and micron-SV study, we claim that the former gives the actual track density information. The different track densities and absorbed doses of compound particles in the nucleus together result in the dramatic difference on macroscopic biological response of the two drugs. G. Famulari et al. also illustrated that the nanoscale study better corresponds to the biological response (Famulari et al., 2018).

4 Discussion

BNCT microdosimetric analysis based on the Monte Carlo track structure simulation was conducted in this study. Although previous research has reported that condensed history algorithms can approximate the result of track structure simulation when the step size and production cut are set to an optimized value, further studies are still needed to prove this argument when using smaller SV (Kyriakou et al., 2017; Kyriakou et al., 2019; Lazarakis et al., 2018). When the step size for the condensed history algorithm is artificially specified (Kyriakou et al., 2021a), the upper limit of step size is fixed, which means one step with a longer length than the fixed step size in the track structure simulation will be split into several steps in the condensed history algorithm. This kind of processing is error-prone in the case of a large span of the step size and small SV. For nanoscopic particle transport, track structure simulation is more advantageous because it is a "step-by-step" method. That means there is no association of multiple processes viewed as one step, which is always used to improve the calculation efficiency in MCCH simulation. In addition, there is no need to set limits such as step size and production cut artificially in MCTS simulation.

In recent years, many publications have started using nano-SV to calculate the classical microdosimetric parameters such as lineal energy and specific energy, and they classified their work as microdosimetry (Famulari et al., 2018; Kyriakou et al., 2021b). Nanoscale research has its unique value. Microdosimetric work aims to reflect the radiation quality or biological effect via the local energy deposition distribution (i.e., lineal energy and specific energy spectra). The SV at the micrometer level represents biological structures at the cellular and subcellular scale, e.g., the cell nucleus; the SV at the nanometer level represents the chromosome or DNA since the radius of the DNA double helix is approximately 1 nm. Some research on photon, alpha, electron, and neutron declared that nano-SV might describe more fundamental damage mechanisms and can lead to more accurate descriptors of the relative biological effectiveness (Famulari et al., 2018; Lillhök et al., 2007; Mazzucconi et al., 2019a).

The key to performing the track structure simulation is the accuracy of the physics cross-sections. This paper reported the first attempt to derive low-energy Lithium ionization cross-sections for MCTS based on the effective charge cross-section scalation method and phenomenological double-parameter modification. This method uses the concept of equivalent charge and weights the Rudd cross-sections of hydrogen and proton in a specific ratio, creating the modified cross-sections for Lithium. As such, since this method does not

introduce physics models for the excitation and charge exchange processes, there would be no Lithium++, Lithium+, and uncharged Lithium created during the whole particle transport. Nevertheless, this approximation has proven accurate enough to reproduce the range and stopping-power data from ICRU_73 below 1 MeV/u compared to existing Geant4 cross-section data (Figure 3). Above this value, in the high energy limit, the introduced parameters λ_1 and λ_2 can overestimate the cross-sections by 10% ($\lambda_1 = 1.1$) and must not be used above 1 MeV/u. Correct predictions of stopping power and range do not fully validate the modified cross-sections of the different Lithium charge states, thus further validation of cross-sections will require the development of precision experimental devices such as nano-dosimeter, which focus on the particle track structure measurements at the DNA level (Conte et al., 2018). In some scenarios, for example, during MRI-guided BNCT, where the accurate particle charge is required to calculate the track structure, this method may not be applicable.

The cell structure (e.g., cell size, cell shape, cell organelle distribution) and the microscopic boron distribution which relies on drug accumulation, can affect the microdosimetric results. The current simulation settings for geometry and source are relatively idealized. Further development of the measurement equipment and techniques for microscopic boron imaging might potentially improve the accuracy of boron distribution at cell or subcellar scales. Besides, specific geometric models should be designed for different cells (McNamara et al., 2018).

Although the current work focused on the lineal energy of different components in BNCT, the MCTS simulation platform can be further used to analyze the biological effects at the DNA scale in BNCT, incorporating physical, chemical, and biological processes. Numerous studies on RBE evaluation via the DNA damage yield have been published in other therapeutic fields (Ganjeh et al., 2021; Nikjoo et al., 2016). We plan to investigate the direct/indirect DNA damage yields and perform a repair analysis in BNCT. The accurate MCTS simulation at the micro- and nano-meter scale reported in this paper is the foundation for future research.

5 Conclusion

This paper reports a BNCT microdosimetric study based on the Monte Carlo track structure simulation toolkit, TOPAS-nBio. We amended the ionization cross-sections for Lithium via the effective charge cross-section scalation method and phenomenological double-parameter modification, and then verified the range and stopping power for Lithium, alpha, and proton with the specific energy scope in BNCT, ensuring the applicability of the physics models and cross-sections. The lineal energy spectra of charged particles in BNCT were calculated, and the influence of sensitive volume (SV) size was discussed. MCCH obtained similar results to MCTS when using micron-SV, while overestimating the lineal energy when using Nano-SV. Besides, we found that the microscopic boron distribution can significantly affect the lineal energy for Lithium, while the effect for alpha is minimal. Similar results to PHITS simulation with micron-SV were obtained for the compound particles and monoenergetic protons. The spectra of the compound particles with nano-SV reflected the different track densities in cell nucleus when using different boron drugs. However, this cannot yet be

directly used to explain the experimentally different RBE/CBE of BPA and BSH because the relationship between $\bar{y}_D$ and the macroscopic biological response is not straightforward. This work and the developed methodology could impact the research fields in BNCT where understanding radiation effects is crucial, such as the treatment planning system, source evaluation, and new boron drug development.

Acknowledgement

7 References

Barkas WH, 1963. Nuclear Research Emulsions: Particle behavior and emulsion applications, edited by Evans DA. Academic Press.

Bernal MA, Bordage MC, Brown JMC, Davídková M, Delage E, El Bitar Z, Enger SA, Francis Z, Guatelli S, Ivanchenko VN, 2015. Track structure modeling in liquid water: A review of the Geant4-DNA very low energy extension of the Geant4 Monte Carlo simulation toolkit. Physica Medica 31, 861–874. [PubMed: 26653251]

Burmeister J, Kota C, Maughan RL, Waker AJ, 2001. Miniature tissue-equivalent proportional counters for BNCT and BNCEFNT dosimetry. Medical physics 28, 1911–1925. [PubMed: 11585222]

Capala J, Makar MS, Coderre JA, 1996. Accumulation of boron in malignant and normal cells incubated in vitro with boronophenylalanine, mercaptoborane or boric acid. Radiation research 146, 554–560. [PubMed: 8896582]

Colautti P, Moro D, Chiriotti S, Conte V, Evangelista L, Altieri S, Bortolussi S, Protti N, Postuma I, 2014. Microdosimetric measurements in the thermal neutron irradiation facility of LENA reactor. Applied Radiation and Isotopes 88, 147–152. [PubMed: 24508176]

Conte V, Selva A, Colautti P, Hilgers G, Rabus H, Bantsar A, Pietrzak M, Pszona S, 2018. Nanodosimetry: towards a new concept of radiation quality. Radiation protection dosimetry 180, 150–156. [PubMed: 29036364]

D-Kondo N, Moreno-Barbosa E, Št phán V, Stefanová K, Perrot Y, Villagrasa C, Incerti S, Alonso BDC, Schuemann J, Faddegon B, 2021. DNA damage modeled with Geant4-DNA: effects of plasmid DNA conformation and experimental conditions. Physics in Medicine & Biology 66, 245017.

Famulari G, Pater P, Enger SA, 2018. Microdosimetric evaluation of current and alternative brachytherapy sources—a Geant4-DNA simulation study. International Journal of Radiation Oncology* Biology* Physics 100, 270–277.

Francis Z, Incerti S, Ivanchenko V, Champion C, Karamitros M, Bernal M.a., El Bitar Z, 2011. Monte Carlo simulation of energy-deposit clustering for ions of the same LET in liquid water. Physics in Medicine & Biology 57, 209.

Fukuda H, 2021. Response of Normal Tissues to Boron Neutron Capture Therapy (BNCT) with B-10-Borocaptate Sodium (BSH) and B-10-Paraboronophenylalanine (BPA). Cells 10.

Furuta T, Sato T, 2021. Medical application of particle and heavy ion transport code system PHITS. Radiological Physics and Technology 14, 215–225. [PubMed: 34195914]

Ganjeh ZA, Eslami-Kalantari M, Loushab ME, Mowlavi AA, 2021. Calculation of direct DNA damages by a new approach for carbon ions and protons using Geant4-DNA. Radiation Physics and Chemistry 179, 109249.

Hopewell J, Morris G, Schwint A, Coderre J, 2011. The radiobiological principles of boron neutron capture therapy: a critical review. Applied Radiation and Isotopes 69, 1756–1759. [PubMed: 21543233]

Horiguchi H, Sato T, Kumada H, Yamamoto T, Sakae T, 2015. Estimation of relative biological effectiveness for boron neutron capture therapy using the PHITS code coupled with a microdosimetric kinetic model. Journal of radiation research 56, 382–390. [PubMed: 25428243]

Hu N, Tanaka H, Takata T, Endo S, Masunaga S, Suzuki M, Sakurai Y, 2020a. Evaluation of PHITS for microdosimetry in BNCT to support radiobiological research. Applied Radiation and Isotopes 161, 109148. [PubMed: 32250844]

Hu N, Tanaka H, Takata T, Okazaki K, Uchida R, Sakurai Y, 2020b. Microdosimetric quantities of an accelerator-based neutron source used for boron neutron capture therapy measured using a gas-filled proportional counter. Journal of radiation research 61, 214–220. [PubMed: 32030430]

Hu N, Uchida R, Tran LT, Rosenfeld A, Sakurai Y, 2018. Feasibility study on the use of 3D silicon microdosimeter detectors for microdosimetric analysis in boron neutron capture therapy. Applied Radiation and Isotopes 140, 109–114. [PubMed: 30015038]

Incerti S, Baldacchino G, Bernal M, Capra R, Champion C, Francis Z, Gueye P, Mantero A, Mascialino B, Moretto P, 2010a. The geant4-dna project. International Journal of Modeling, Simulation, and Scientific Computing 1, 157–178.

Incerti S, Ivanchenko A, Karamitros M, Mantero A, Moretto P, Tran H, Mascialino B, Champion C, Ivanchenko V, Bernal M, 2010b. Comparison of GEANT4 very low energy cross section models with experimental data in water. Medical physics 37, 4692–4708. [PubMed: 20964188]

Incerti S, Kyriakou I, Bernal M, Bordage M, Francis Z, Guatelli S, Ivanchenko V, Karamitros M, Lampe N, Lee SB, 2018. Geant4-DNA example applications for track structure simulations in liquid water: A report from the Geant4-DNA Project. Medical physics 45, e722–e739.

Islam MM, Lertnaisat P, Meesungnoen J, Sanguanmith S, Jay-Gerin J-P, Katsumura Y, Mukai S, Umehara R, Shimizu Y, Suzuki M, 2017. Monte Carlo track chemistry simulations of the radiolysis of water induced by the recoil ions of the 10 B (n, α) 7 Li nuclear reaction. 1. Calculation of the yields of primary species up to 350° C. Rsc Advances 7, 10782–10790.

Kyriakou I, Emfietzoglou D, Ivanchenko V, Bordage M, Guatelli S, Lazarakis P, Tran H, Incerti S, 2017. Microdosimetry of electrons in liquid water using the low-energy models of Geant4. Journal of Applied Physics 122, 024303.

Kyriakou I, Ivanchenko V, Sakata D, Bordage M, Guatelli S, Incerti S, Emfietzoglou D, 2019. Influence of track structure and condensed history physics models of Geant4 to nanoscale electron transport in liquid water. Physica Medica 58, 149–154. [PubMed: 30642767]

Kyriakou I, Sakata D, Tran HN, Perrot Y, Shin W-G, Lampe N, Zein S, Bordage MC, Guatelli S, Villagrasa C, 2021a. Review of the geant4-dna simulation toolkit for radiobiological applications at the cellular and dna level. Cancers 14, 35. [PubMed: 35008196]

Kyriakou I, Tremi I, Georgakilas AG, Emfietzoglou D, 2021b. Microdosimetric investigation of the radiation quality of low-medium energy electrons using Geant4-DNA. Applied Radiation and Isotopes 172, 109654. [PubMed: 33676082]

Lazarakis P, Incerti S, Ivanchenko V, Kyriakou I, Emfietzoglou D, Corde S, Rosenfeld AB, Lerch M, Tehei M, Guatelli S, 2018. Investigation of track structure and condensed history physics models for applications in radiation dosimetry on a micro and nano scale in Geant4. Biomedical Physics & Engineering Express 4, 024001.

Lillhök JE, Grindborg J-E, Lindborg L, Gudowska I, Carlsson GA, Söderberg J, Kope M, Medin J, 2007. Nanodosimetry in a clinical neutron therapy beam using the variance-covariance method and Monte Carlo simulations. Physics in Medicine & Biology 52, 4953. [PubMed: 17671346]

Matsumoto Y, Fukumitsu N, Ishikawa H, Nakai K, Sakurai H, 2021. A critical review of radiation therapy: from particle beam therapy (proton, carbon, and BNCT) to beyond. Journal of Personalized Medicine 11, 825. [PubMed: 34442469]

Matsuya Y, Kai T, Sato T, Ogawa T, Hirata Y, Yoshii Y, Parisi A, Liamsuwan T, 2022. Track-structure modes in particle and heavy ion transport code system (PHITS): application to radiobiological research. International Journal of Radiation Biology 98, 148–157. [PubMed: 34930091]

Mazzucconi D, Bortot D, Agosteo S, Pola A, Pasquato S, Fazzi A, Colautti P, Conte V, Petringa G, Amico A, 2019a. Microdosimetry at nanometric scale with an avalanche-confinement tepc: response against a helium ion beam. Radiation Protection Dosimetry 183, 177–181. [PubMed: 30535177]

Mazzucconi D, Bortot D, Pola A, Fazzi A, Colautti P, Conte V, Petringa G, Cirrone G, Agosteo S, 2019b. Nano-microdosimetric investigation at the therapeutic proton irradiation line of CATANA. Radiation Measurements 123, 26–33.

McNamara AL, Ramos-Méndez J, Perl J, Held K, Dominguez N, Moreno E, Henthorn NT, Kirkby KJ, Meylan S, Villagrasa C, 2018. Geometrical structures for radiation biology research as implemented in the TOPAS-nBio toolkit. Physics in Medicine & Biology 63, 175018. [PubMed: 30088810]

Moss RL, 2014. Critical review, with an optimistic outlook, on Boron Neutron Capture Therapy (BNCT). Applied Radiation and Isotopes 88, 2–11. [PubMed: 24355301]

Mukawa T, Matsumoto T, Niita K, 2011. Study on microdosimetry for boron neutron capture therapy. Progress in Nuclear Science and Technology 2, 242–246.

Nelder J, 1965. A. & Mead R(1965). Computer J 7, 308–313.

Nikjoo H, Taleei R, Liamsuwan T, Liljequist D, Emfietzoglou D, 2016. Perspectives in radiation biophysics: from radiation track structure simulation to mechanistic models of DNA damage and repair. Radiation Physics and Chemistry 128, 3–10.

Parisi A, Furutani KM, Beltran CJ, 2022. On the calculation of the relative biological effectiveness of ion radiation therapy using a biological weighting function, the microdosimetric kinetic model (MKM) and subsequent corrections (non-Poisson MKM and modified MKM). Physics in Medicine & Biology 67, 095014.

Qi J, Geng C, Tang X, Tian F, Han Y, Liu H, Liu Y, Bortolussi S, Guan F, 2021. Effect of spatial distribution of boron and oxygen concentration on DNA damage induced from boron neutron capture therapy using Monte Carlo simulations. International journal of radiation biology 97, 986–996. [PubMed: 33970761]

Sato T, Masunaga S. i., Kumada H, Hamada N, 2018. Microdosimetric modeling of biological effectiveness for boron neutron capture therapy considering intra-and intercellular heterogeneity in 10B distribution. Scientific reports 8, 1–14. [PubMed: 29311619]

Schmitt E, Friedland W, Kundrát P, Dingfelder M, Ottolenghi A, 2015. Cross-section scaling for track structure simulations of low-energy ions in liquid water. Radiation protection dosimetry 166, 15–18. [PubMed: 25969528]

Schuemann J, McNamara A, Ramos-Méndez J, Perl J, Held K, Paganetti H, Incerti S, Faddegon B, 2019. TOPAS-nBio: an extension to the TOPAS simulation toolkit for cellular and sub-cellular radiobiology. Radiation research 191, 125–138. [PubMed: 30609382]

Seltzer S, Fernandez-Varea J, Andreo P, Bergstrom P, Burns D, Krajcar Broni I, Ross C, Salvat F, 2016. Key data for ionizing-radiation dosimetry: measurement standards and applications, ICRU Report 90.

Selva A, Bellan L, Bianchi A, Giustiniani G, Colautti P, Fagotti E, Pisent A, Conte V, 2022. Microdosimetry of an accelerator based thermal neutron field for Boron Neutron Capture Therapy. Applied Radiation and Isotopes 182, 110144. [PubMed: 35168037]

Sigmund P, Bimbot R, Geissel H, 2005. Stopping of ions heavier than helium. ICRU report 73. J. Int. Comm. Radiat. Units Meas 5.

Suzuki M, 2020. Boron neutron capture therapy (BNCT): A unique role in radiotherapy with a view to entering the accelerator-based BNCT era. International journal of clinical oncology 25, 43–50. [PubMed: 31168726]

Thompson SJ, Rooney A, Prise KM, McMahon SJ, 2022. Evaluating Iodine-125 DNA Damage Benchmarks of Monte Carlo DNA Damage Models. Cancers 14, 463. [PubMed: 35158731]

Wu S, Geng C, Tang X, Bortolussi S, Han Y, Shu D, Gong C, Zhang X, Tian F, 2020. Dosimetric impact of respiratory motion during boron neutron capture therapy for lung cancer. Radiation Physics and Chemistry 168, 108527.
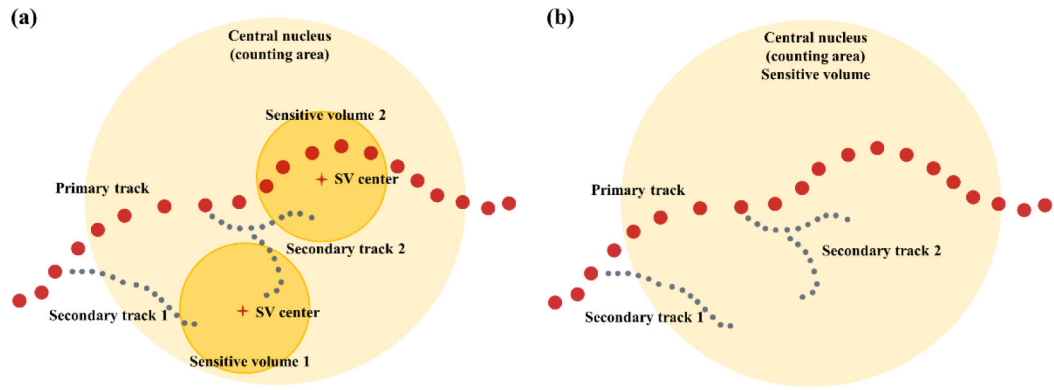
Highlights

The new Lithium cross-sections for MCTS simulation are calculated and verified.

A significant difference in y spectra for Lithium is observed when using nano-SV.

$\overline{y}_D$ for BPA and BSH is 158.35 and 132.47 keV/μm with nano-SV, respectively.
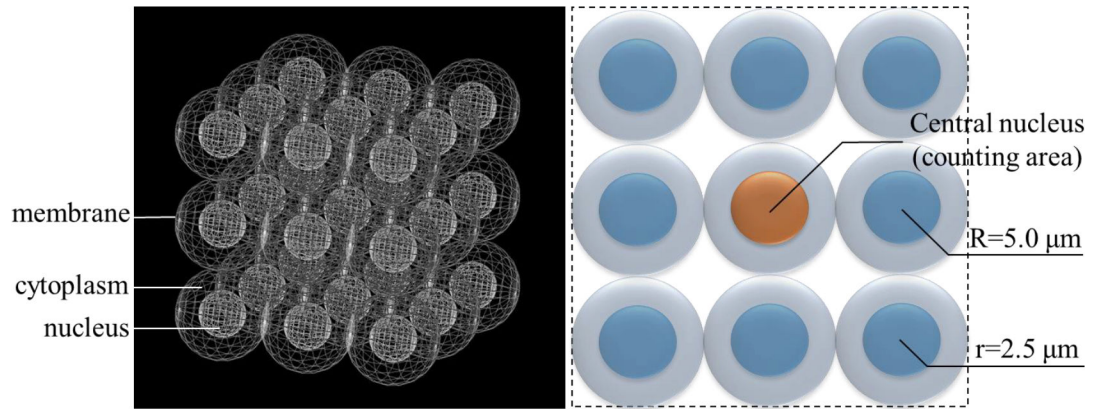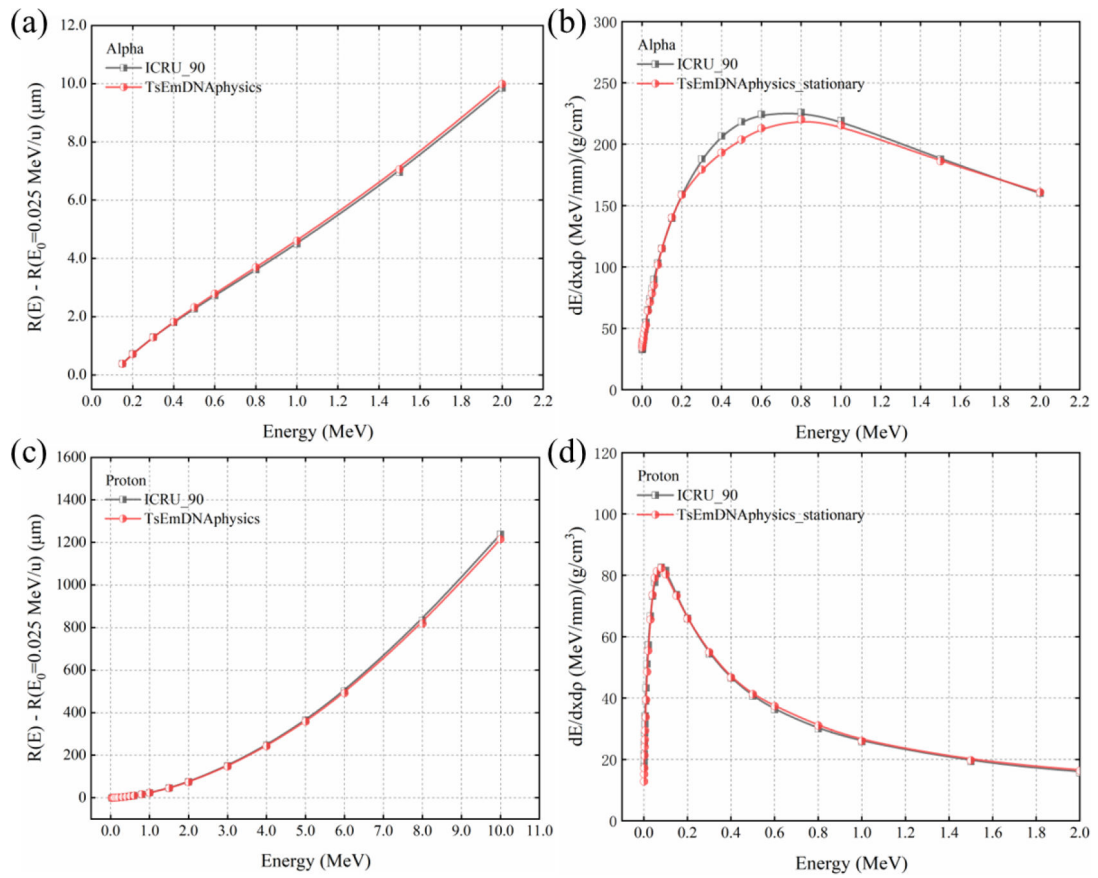
Figure 1.
Geometric model for lineal energy calculation shown in Qt5 and its sectional view

Figure 2.
Schematic of lineal energy calculation: (a) nano-SV (radius = 1 nm) (b) micron-SV (radius = 2.5 μm). The volumes of SVs and nuclei are for visual display and do not represent the actual size.
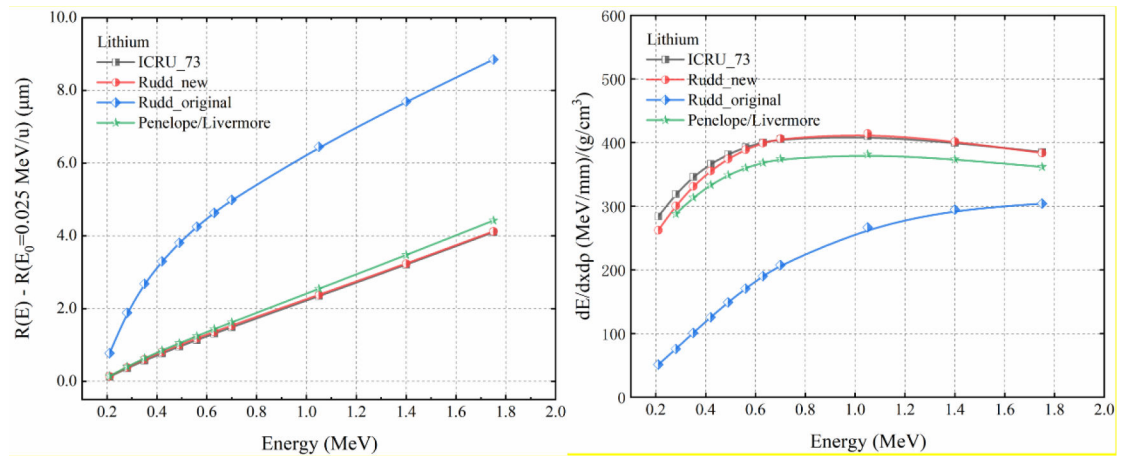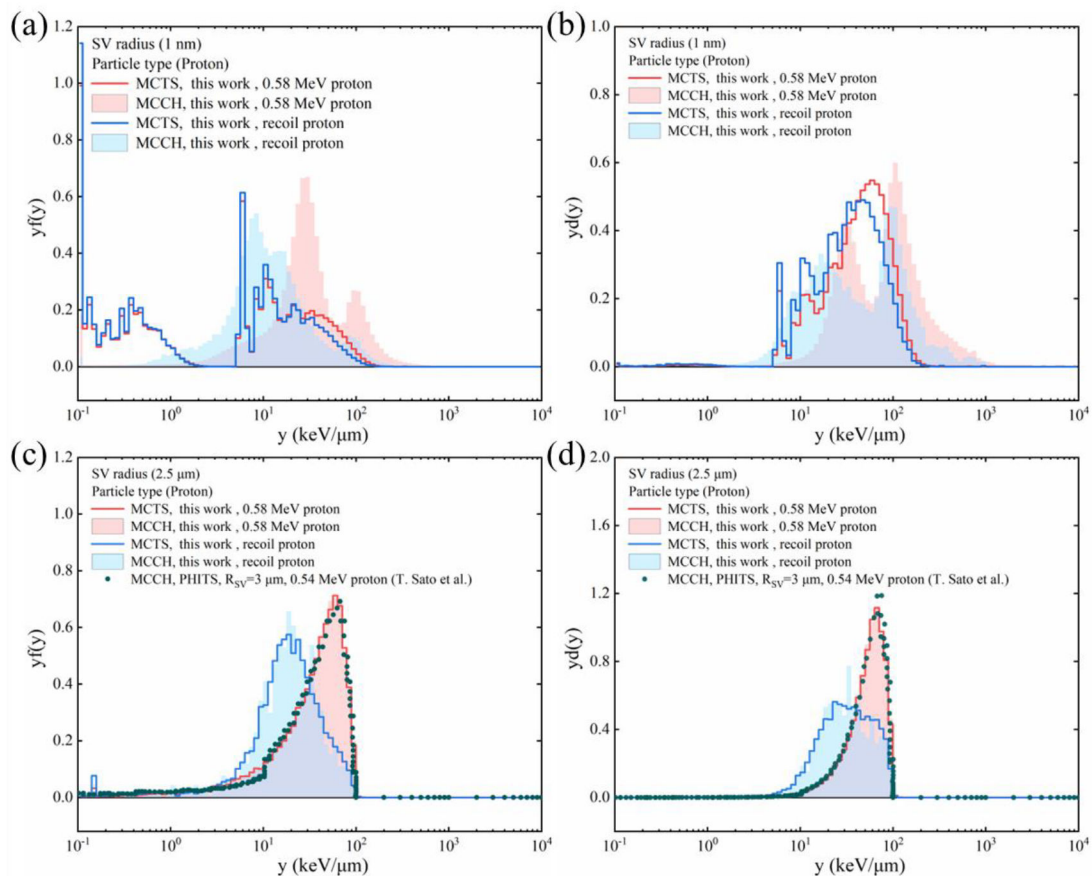
Figure 3.
Range and stopping power of Lithium in the liquid water calculated with different cross-sections or physics models
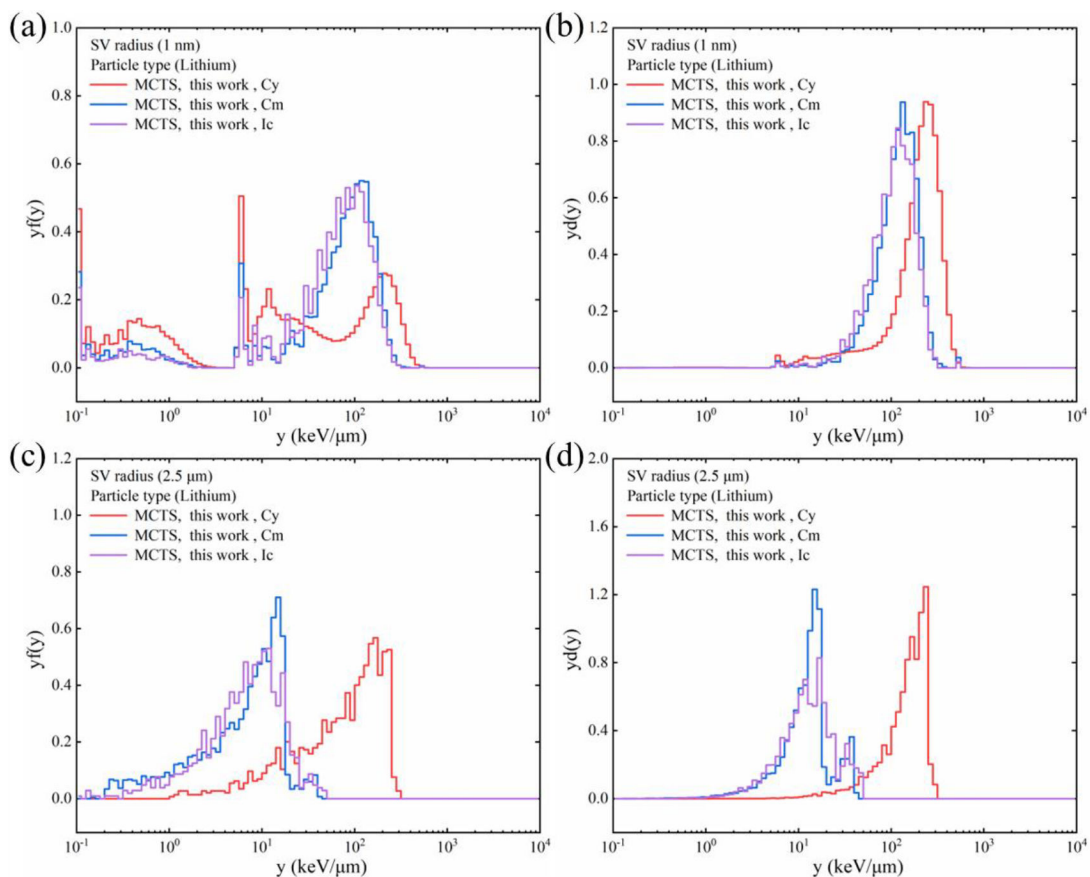
Figure 4.
Range and stopping power of alpha and proton in the liquid water calculated with "TsEmDNAphysics" or "TsEmDNAphysics_stationary"
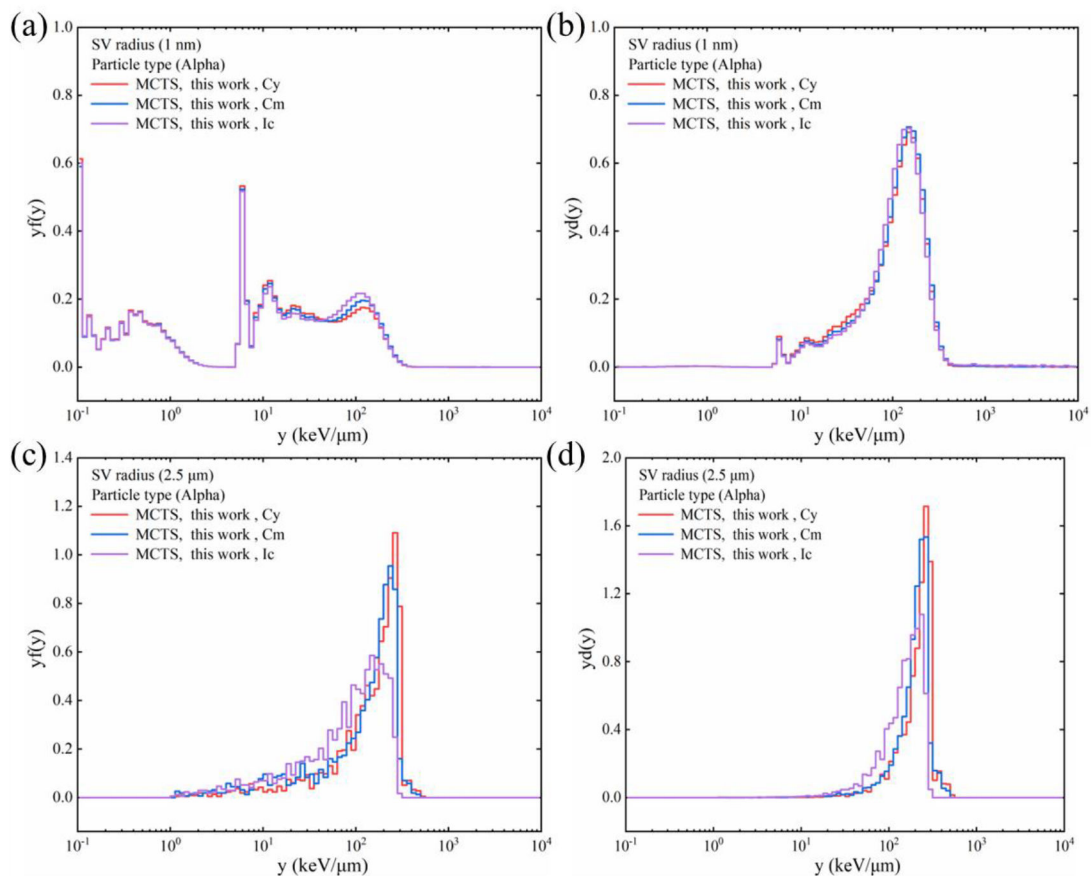
Figure 5.
The lineal energy spectra of protons: (a) SV radius = 1 nm, frequency spectrum; (b) SV radius = 1 nm, dose contribution spectrum (c) SV radius = 2.5 μm, frequency spectrum; (d) SV radius = 2.5 μm, dose contribution spectrum. The solid line represents the results of MCTS, while the color block represents the results of MCCH (G4-Livermore). Red represents the results of monoenergetic proton (from $^{14}N(n,p)^{14}C$ reaction), and blue represents the results of recoil proton (from $^{1}H(n,n)p$ reaction). Green points are data from the published work by T. Sato et al through PHITS simulation.
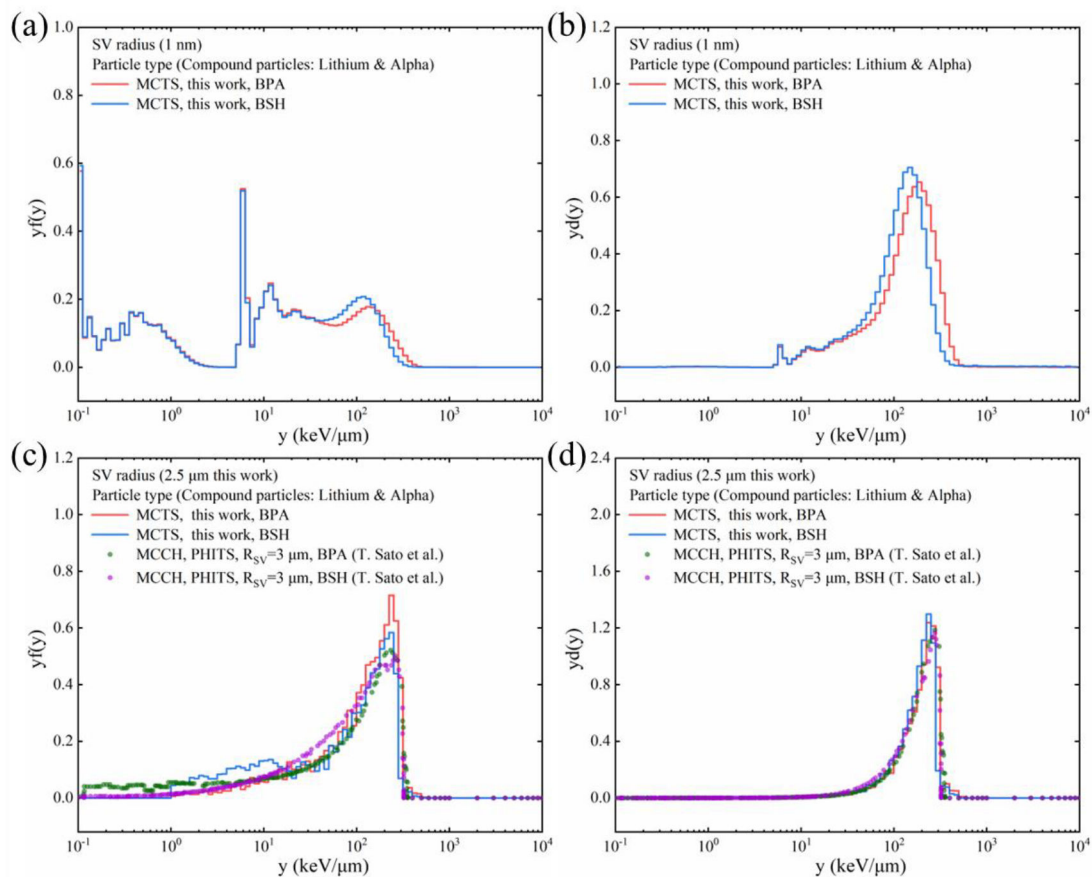
Figure 6.
The lineal energy spectra of Lithium: (a) SV radius = 1 nm, frequency spectrum; (b) SV radius = 1 nm, dose contribution spectrum (c) SV radius = 2.5 μm, frequency spectrum; (d) SV radius = 2.5 μm, dose contribution spectrum. Solid lines with different colors represent the spectra under different source conditions (i.e., red: Cy, blue: Cm, purple: Ic).

Figure 7.
The lineal energy spectra of alpha: (a) SV radius = 1 nm, frequency spectrum; (b) SV radius = 1 nm, dose contribution spectrum (c) SV radius = 2.5 μm, frequency spectrum; (d) SV radius = 2.5 μm, dose contribution spectrum. Solid lines with different colors represent the spectra under different source conditions (i.e., red: *Cy*, blue: *Cm*, purple: *Ic*).

Figure 8.
The lineal energy spectra for the compound particles (Lithium and alpha) in BNCT: (a) SV radius = 1 nm, frequency spectrum; (b) SV radius = 1 nm, dose contribution spectrum (c) SV radius = 2.5 μm, frequency spectrum; (d) SV radius = 2.5 μm, dose contribution spectrum. Different colors represent the results under different boron distributions of this work and data by PHITS simulation (Sato et al., 2018) (i.e., red line: BPA this work, blue line: BSH this work, green point: BPA PHITS, purple point: BSH PHITS).

Table 1.

Physics models in "TsEmDNAphysics"

	Elastic scattering	Excitation	Ionization	Others
Electron	G4DNAChampionElasticModel (7.4 eV-1 MeV)	G4DNABornExcitationMode (9 eV-1 MeV)	G4DNABornIonisationModel (11 eV-1 MeV)	G4DNASancheExcitationMo... eV-100 eV) G4DNAMeltonAttachmentMo... eV-13 eV)
Proton	G4DNAIonElasticModel(100 eV-1 MeV)	G4DNAMillerGreenExcitationModel (10 eV-500 keV) G4DNABornExcitationModel (500 keV-100 MeV)	G4DNARuddIonisationModel (100 eV-500 keV) G4DNABornIonisationMode (500 keV-100 MeV)	G4DNADingfelderChargeDecrea... (100 eV-100 MeV)
Hydrogen	G4DNAIonElasticModel (100 eV-1 MeV)	G4DNAMillerGreenExcitationModel (10 eV-500 keV)	G4DNARuddIonisationModel (100 eV-100 MeV)	G4DNADingfelderChargeIncrea... (100 eV-100 MeV)
AlphaAlpha+Helium	G4DNAIonElasticModel (100 eV-1 MeV)	G4DNAMillerGreenExcitationModel (1 keV-400 MeV)	G4DNARuddIonisationModel (1 keV-400 MeV)	G4DNADingfelderChargeDecrea... (1 keV-400 MeV) [alpha++ and ... G4DNADingfelderChargeIncrea... (1 keV-400 MeV) [alpha+ and h...
Heavyions	-	-	TsDNARuddIonisationExtendedModel (0.025 MeV/u-1E6MeV/u)	-
Gamma	G4Livermore (PhotoElectricEffect, ComptonScattering, and GammaConversion)			

Table 2.

Weighting factors for Eq. (7)

		BPA	BSH
	Ic	0.2214	0.5141
Q	Cy	0.7786	-
	Cm	-	0.4859

Table 3

Frequency-mean lineal energy ($\bar{y}_F$) and dose-mean lineal energy ($\bar{y}_D$) of proton in BNCT

	Nano-SV			
	MCTS		MCCH (G4-Livermore)	
	$\bar{y}_F$(keV/μm)	$\bar{y}_D$(keV/um)	$\bar{y}_F$(keV/μm)	$\bar{y}_D$(keV/μm)
0.58 MeV proton	15.67±0.02	52.40±0.57	47.09±0.18	123.29±1.61
Recoil proton	12.00±0.09	41.35±0.59	20.58±0.55	78.69±2.52

	Micron-SV			
	MCTS		MCCH (G4-Livermore)	
	$\bar{y}_F$(keV/μm)	$\bar{y}_D$(keV/μm)	$\bar{y}_E$(keV/μm)	$\bar{y}_D$(keV/μm)
0.58 MeV proton	40.60±0.47	55.49±0.78	40.95±0.67	55.57±1.14
Recoil proton	23.51±0.47	37.43±0.99	23.30±1.68	36.13±4.11

Table 4

Frequency-mean lineal energy ($\bar{y}_F$) and dose-mean lineal energy ($\bar{y}_D$) of Lithium and alpha in BNCT

	Nano-SV			
	Lithium		Alpha	
	$\bar{y}_F$(keV/μm)	$\bar{y}_D$(keV/μm)	$\bar{y}_E$(keV/μm)	$\bar{y}_D$(keV/μm)
Cy	68.80±0.25	210.37±0.99	35.41±0.06	130.93±1.69
Cm	78.01±2.04	128.47±4.99	38.43±0.11	140.79±9.01
Ic	72.89±3.37	116.55±7.67	39.32±0.15	149.19±6.99
	Micron-SV			
	Lithium		Alpha	
	$\bar{y}_F$(keV/μm)	$\bar{y}_D$(keV/μm)	$\bar{y}_E$(keV/μm)	$\bar{y}_D$(keV/μm)
Cy	100.24±5.84	155.20±11.44	169.61±7.76	223.28±11.85
Cm	9.31±0.27	13.92±0.62	149.15±8.29	205.62±14.28
Ic	5.79±1.61	10.97±3.69	108.55±5.31	159.96±9.51

Table 5

Frequency-mean lineal energy ($\bar{y}_F$) and dose-mean lineal energy ($\bar{y}_D$) for the compound particles in BNCT

Nano-SV		
	$\bar{y}_F$(keV/μm)	$\bar{y}_D$(keV/μm)
BPA (this work)	43.82	158.35
BSH (this work)	39.14	132.47
Micron-SV		
	$\bar{y}_F$(keV/μm)	$\bar{y}_\Re$(keV/μm)
BPA (this work)	137.24	199.64
BSH (this work)	106.87	182.73
BPA (T. Sato et al.)	118.43	213.55
BSH (T. Sato et al.)	120.32	198.21